LETTERS
https://doi.org/10.1038/s41550-018-0437-9

nature astronomy

Corrected: Author Correction

Equation of state of iron under core conditions of large rocky exoplanets

Raymond F. Smith[1*], Dayne E. Fratanduono[1], David G. Braun[1], Thomas S. Duffy[2], June K. Wicks[2,3], Peter M. Celliers[1], Suzanne J. Ali[1], Amalia Fernandez-Pañella[1], Richard G. Kraus[1], Damian C. Swift[1], Gilbert W. Collins[1,4] and Jon H. Eggert[1]

The recent discovery of thousands of planets outside our Solar System raises fundamental questions about the variety of planetary types and their corresponding interior structures and dynamics. To better understand these objects, there is a strong need to constrain material properties at the extreme pressures found within planetary interiors[1,2]. Here we used high-powered lasers at the National Ignition Facility to ramp compress iron over nanosecond timescales to 1.4 TPa (14 million atmospheres)—a pressure four times higher than for previous static compression data. A Lagrangian sound-speed analysis was used to determine pressure, density and sound speed along a continuous isentropic compression path. Our peak pressures are comparable to those predicted at the centre of a terrestrial-type exoplanet of three to four Earth masses[3], representing the first absolute equation of state measurements for iron at such conditions. These results provide an experiment-based mass–radius relationship for a hypothetical pure iron planet that can be used to evaluate plausible compositional space for large, rocky exoplanets.

Of the thousands of exoplanets discovered so far, those that are 1–4 times the radius of the Earth are the most abundant[4]. Based on mass and radius determinations, a number of these planets are inferred to have compositions comparable to terrestrial planets within our Solar System[5,6], and are referred to here as super-Earths. As core pressures for even a 5 Earth-mass planet can reach as high as 2 TPa[3], a fundamental requirement for constraining exoplanetary composition and interior structure is an accurate determination of the equation of state (EOS) of planetary materials at TPa pressures. Iron is a cosmochemically abundant element that plays a major part in terrestrial planetary interiors as the dominant core constituent. The ultrahigh pressure properties of iron are of importance for interpreting observational data for large rocky extrasolar planets. Aside from a planet's mass–radius relationship[2], the properties of iron can influence the planet in other important ways. The size of the iron core may affect the production of partial melt (owing to the steepness of the internal pressure gradient), which in turn influences atmospheric formation and evolution[7]. Planetary magnetic fields arising from Fe-rich cores have an important role in the atmospheric evolution and surface environment of planets[8]. The relative size of core and mantle may affect the ability of the planet to initiate plate tectonics. Also, a well constrained Fe EOS is needed for models that describe the removal of mantles through giant impact events[9].

Despite its importance, the behaviour of iron at pressures most relevant for super-Earth cores remains highly uncertain because of the difficulty of experimental study above 0.3 TPa using conventional tools such as the diamond anvil cell[10]. Shock compression experiments can reach higher pressures but, owing to large increases in entropy with pressure, shock temperatures are too high to constrain exoplanet interior conditions. Theoretical approaches for calculating the properties of Fe at TPa pressures are also poorly constrained. First-principles calculations of isothermal cold compression in Fe at high pressures exhibit a large degree of uncertainty owing to the choice of density functionals and the difficulty in modelling the effects of magnetism[11]. A recent theoretical calculation has explored the phase diagram of Fe up to ultrahigh pressures[12]. This study indicates that the hexagonal close-packed (HCP) phase of iron is expected to be stable to 6 TPa and also places constraints on the 0 K iron EOS to ultrahigh pressures[12]. Here, we present ramp compression data of Fe to a pressure of 1.4 TPa (equivalent to 14 million atmospheres of pressure) and 2.6 times compression. Ramp compression produces a near-isentropic loading path, which ensures that Fe stays within the solid state up to very high pressures[13,14]. Exoplanet interior models demonstrate the importance of accurate EOS information for key planetary components[2]. Our work provides direct experimental constraints on the pressure, density, sound speed and Grüneisen parameter of Fe at conditions found deep within super-Earth interiors.

Experiments were conducted at the National Ignition Facility (NIF) located at the Lawrence Livermore National Laboratory. NIF can deliver up to 2 MJ of laser energy over 30 ns and provides the necessary laser power and control to ramp compress materials to TPa pressures[15]. The target design to ramp compress Fe to 1.4 TPa consisted of a ~40-μm-thick Cu foil glued to a stepped Fe sample with four thicknesses—85, 95, 105 and 115 μm (Supplementary Fig. 1a). The energy from 176 laser beams was converted into an X-ray drive, which, through direct ablation of the Cu layer, imparted a monotonically increasing ramp pressure wave into the Cu/Fe sample. Ramp compression waves are unstable and, in compressible materials, steepen with propagation distance owing to the increase of sound speed with pressure. Precise shaping of the laser pulse was used to tailor the temporal profile of the ramp compression wave and avoid the formation of a strong shock and the associated rapid heating that could melt the sample. Once the pressure wave reached the Fe free surface, the sample accelerated. A Doppler velocity interferometer was used to measure the time history of the Fe free-surface velocity, u_{fs}, for each of the four Fe thicknesses (Fig. 1 and Methods). Fe undergoes a body-centred cubic (BCC) to HCP phase transformation with an associated 5% volume collapse at

[1]Lawrence Livermore National Laboratory, Livermore, CA, USA. [2]Department of Geosciences, Princeton University, Princeton, NJ, USA. [3]Department of Earth and Planetary Sciences, Johns Hopkins University, Baltimore, MD, USA. [4]Departments of Mechanical Engineering, Physics and Astronomy, and the Laboratory for Laser Energetics, University of Rochester, Rochester, NY, USA. *e-mail: smith248@llnl.gov

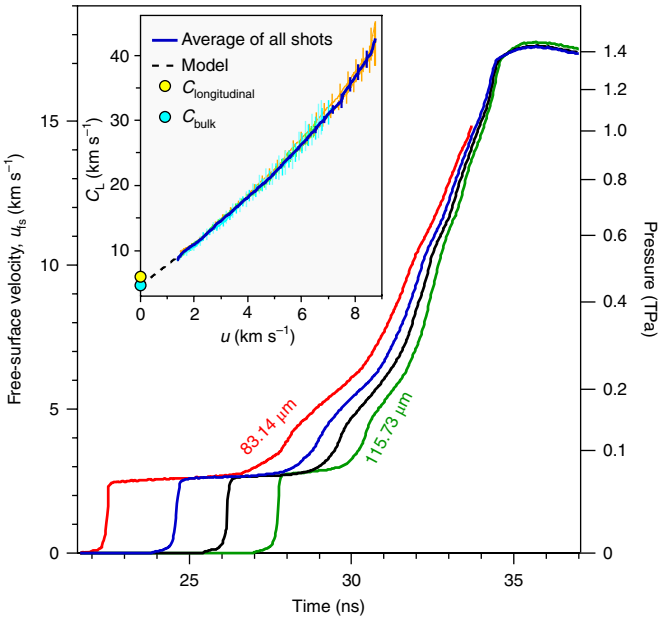

Fig. 1 | Free-surface velocity measurements from a dynamically compressed multi-thickness Fe sample. Doppler interferometry was used to measure free-surface velocity as a function of time, $u_{fs}(t)$, for an Fe sample with four thicknesses: 83.14 μm (red), 96.45 μm (blue), 106.28 μm (black) and 115.73 μm (green). The corresponding bulk sample pressure is plotted on the right-hand axis. The Fe sample was initially shocked to 60 GPa (0.06 TPa) before ramp compression to 1.4 TPa. Inset: Lagrangian sound velocity C_L versus particle velocity u was calculated from velocity versus sample thickness data. Three experiments, each with two independent velocity measurements (green, light blue and light orange lines) yielded C_L data and their average (dark blue line), which were used to determine isentropic P–ρ (see dark blue curve in Fig. 2). Error bars: 1σ. Also shown are the ambient-pressure longitudinal and bulk sound speeds of BCC Fe (yellow and cyan circles)[19] and a low-pressure $C_L(u)$ model used in the Lagrangian analysis (see Methods).

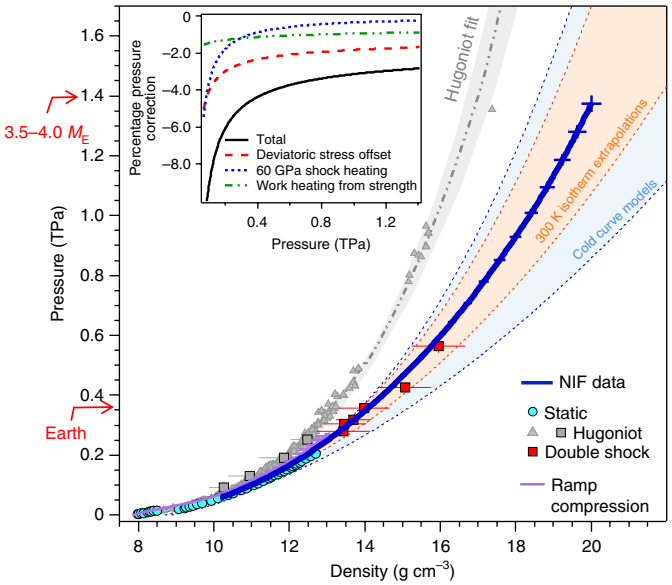

Fig. 2 | Isentropic P–ρ path of Fe to 3.7 Earth-mass planet core conditions. Weighted average of pressure versus density with experimental uncertainties (bold blue curve). Error bars: 1σ. Hugoniot data are shown as grey triangles[18] and squares[17]. Double-shock data are shown as red squares[17]. A fit to the Hugoniot data (grey dashed–dotted line) with uncertainties (grey shaded region) is described in Supplementary Fig. 4. Also plotted are previous ramp compression data[19] (purple curve) and static diamond anvil cell data (light blue circles)[10]. The ranges of EOS extrapolations of low-pressure static data (orange shaded region) and first-principles cold curve calculations (light blue shaded region) represent the uncertainty in the EOS of Fe at TPa pressures (see Supplementary Fig. 5 for a data review). Central pressures for Earth and a 3.5–4.0 Earth-mass (M_E) planet are shown for reference. Inset: the total percentage pressure correction to measured data (black curve) is the sum of corrections for thermal pressure from initial 60 GPa shock (blue dotted line), deviatoric stress offset (red dashed line) and work heating associated with high-pressure Fe strength (green dashed–dotted line) (see Methods for details).

13 GPa[16]. To avoid complexities associated with this transition, the sample was initially shocked to 60 GPa (0.06 TPa), directly into the HCP phase, before ramp compression to TPa pressures.

A Lagrangian analysis was used to transform the measured $u_{fs}(t)$ velocity data into a continuous stress–density (P_x–ρ) and Lagrangian sound speed $C_L(u)$ path, where u is the particle velocity[15]. In all, three shots gave independent $C_L(u)$ and P_x–ρ data. $C_L(u)$ data for these shots are shown as an inset in Fig. 1. C_L and its uncertainty were obtained from thickness and velocity-versus-time data by linear regression using errors determined by our measurement accuracies. The uncertainty was propagated by calculating the weighted mean of all three shots, as shown by the blue curve in the inset of Fig. 1 (see Methods). Owing to a uniaxial compression geometry in our experiments, we measured longitudinal stress, P_x. To transform the measured P_x–ρ path to an isentropic pressure–density (P–ρ) path, it was necessary to correct for (1) the thermal pressure of the initial shock, (2) work heating due to the high-pressure strength of Fe and (3) the deviatoric stress offset associated with relating the measured longitudinal stress to an equivalent hydrostatic pressure. For (2) and (3), we used a high-pressure strength model for Fe (see Methods and Supplementary Figs. 2 and 3). These three corrections, as a function of pressure, are shown in the inset of Fig. 2 and constitute around −2.8% pressure offset at 1.4 TPa. The NIF data reduced to an isentrope is plotted as the bold blue curve in Fig. 2 (see also Supplementary Table 1a). Also plotted are static compression data[10] and extrapolations of static data (orange shaded region) using semi-empirical EOSs (see also Supplementary Fig. 5a). First-principles calculations describing the high-pressure isothermal cold compression of Fe are represented as the light blue shaded region (see Supplementary Fig. 5b). Also plotted are P_x–ρ points determined from extended X-ray absorption fine structure measurements on shock and multi-shock compressed Fe[17], shock Hugoniot[18] and previous low-pressure ramp compression data[19]. In our experiments, Fe was compressed to 20 g cm^{-3}—a 2.5-fold increase over its ambient density. The peak pressure reached the equivalent of that expected at the centre of a 3.5–4.0 Earth-mass terrestrial-type planet[3]. At this density, the extrapolation from static compression experiments using semi-empirical EOSs results in a large pressure uncertainty of ±240 GPa, compared with ±26 GPa for our data. Thus, our work provides a dramatic improvement in experimental constraints on the iron EOS at these extreme conditions. A Vinet fit[20] was used to describe the isentrope (bold blue curve in Fig. 2). The fitting form was $P(X)=3K_0X^{-2}(1-X)\ \exp((1.5K_0'-1.5)(1-X))$, where $X=(\rho_{\epsilon,0}/\rho)^{1/3}$, $\rho_{\epsilon,0}$ is the density at $P=0$ for the Fe ϵ-phase (8.43 g cm^{-3}),[21] and the best-fit parameters are $K_0=177.7(6)$ GPa and $K_0'=5.64(1)$. We note that an extrapolation of our P–ρ fit is in good agreement with values (6 TPa and 33.9 g cm^{-3}) predicted theoretically at the predicted limit of 0 K stability of the HCP phase[12]. This agreement between theory and experimental results provides enhanced confidence in the validity of the current understanding of the EOS of iron for exoplanet modelling.

The isentropic Eulerian bulk sound speed, $C_E^S = \frac{\rho_0}{\rho} C_L^S = \sqrt{\frac{\delta P}{\delta \rho}}\Big|_S$, obtained from our data is plotted as a function of density as the blue curve in Fig. 3. Here, S denotes isentropic compression and ρ_0 is the density of Fe at 1 bar. Our sound speed data indicate that Birch's law (a linear dependence of sound speed on density[22]) holds for Fe to TPa pressures. The inset in Fig. 3a shows the pressure–temperature (P–T) phase diagram for Fe with solid–solid phase boundaries, the melting curve[19], the calculated geotherm for a 5 Earth-mass planet[1] and the calculated Hugoniot path[23]. The dashed blue curve is the calculated isentropic P–T path from an initial 60 GPa shock state and represents the coolest possible compression path in our experiments. Radiation hydrodynamic simulations that calculate direct X-ray heating and thermal conduction from the ablation surface confirm that the Fe sample remains close to room temperature before the onset of dynamic compression. Upon compression, the major contribution to sample temperature is due to a combination of heating from the initial 60 GPa shock and plastic work heating due to the high-pressure strength of Fe[17]. The solid blue region is the estimated range of temperatures associated with work heating from the strength models described in the Methods and Supplementary Fig. 2b,c. Here, the upper temperature limit is calculated with the strength model used in the P–ρ analysis in Fig. 2, and the lower temperature limit represents the heating that results if we consider a strength model based on extrapolated static data. EOS models show that variations in temperature over the range plotted in Fig. 3a have a negligible effect on the estimated pressure and density at several TPa (see Methods and Supplementary Fig. 7).

Comparison between the measured isentrope and a fit to the Hugoniot data (Fig. 2) allows us to provide an experimental constraint of the Grüneisen parameter, γ, for Fe at TPa pressures (Fig. 3b) (see Methods for details). γ is a fundamental thermodynamic quantity with wide applications[23–25]. In planetary cores, it affects the adiabatic temperature gradient and the amount of heat conducted along the adiabat. Relative to Earth, the low values of γ at super-Earth core pressures may result in a lower adiabatic gradient and less heat conducted from the core into the mantle. Knowledge of γ allows us to calculate the bulk sound speed along the Hugoniot, C_E^H, which is in good agreement with previous shock melt data (Fig. 3a and Methods).

Interpretation of the composition and structure of exoplanets is often achieved through comparison of observational measurements of mass and radius with calculated mass–radius curves of the expected constituent materials[2,26–28]. However, these interpretations rely on the accuracy of the EOS models used. Following the analysis of ref. [2], the P–ρ isentrope in Fig. 2 was used to calculate the mass–radius relationship for a homogeneous iron planet, shown as the bold blue curve in Fig. 4 along with mass–radius relationships for theoretical homogeneous planets comprised of H_2O and MgO. Extrapolation of the NIF data assumes the Birch's law fit established in Fig. 3a (faint blue curve). The grey circles represent selected measurements of transiting super-Earth planets with their reported uncertainties[29]. The orange and blue shaded regions represent the range of extrapolations from low-pressure 300 K isotherm measurements of Fe and the range of first-principles isothermal cold curve calculations, respectively (see Supplementary Fig. 5). Earlier studies have suggested that there may be some enigmatic planets with densities greater than that of a pure iron planet[30]. In the size range up to 10 Earth masses we do not find any evidence to confirm the existence of such planets, although this cannot be completely ruled out for a few planets with large mass uncertainties (Fig. 4). Pure iron planets are considered unlikely, based on considerations of physical processes during planetary formation and evolution[31]. Representative previously reported mass–radius curves for an iron planet are also plotted[2,26–28]. These studies are usually based on extrapolations of low-pressure data and produce a wide range of mass–radius curves

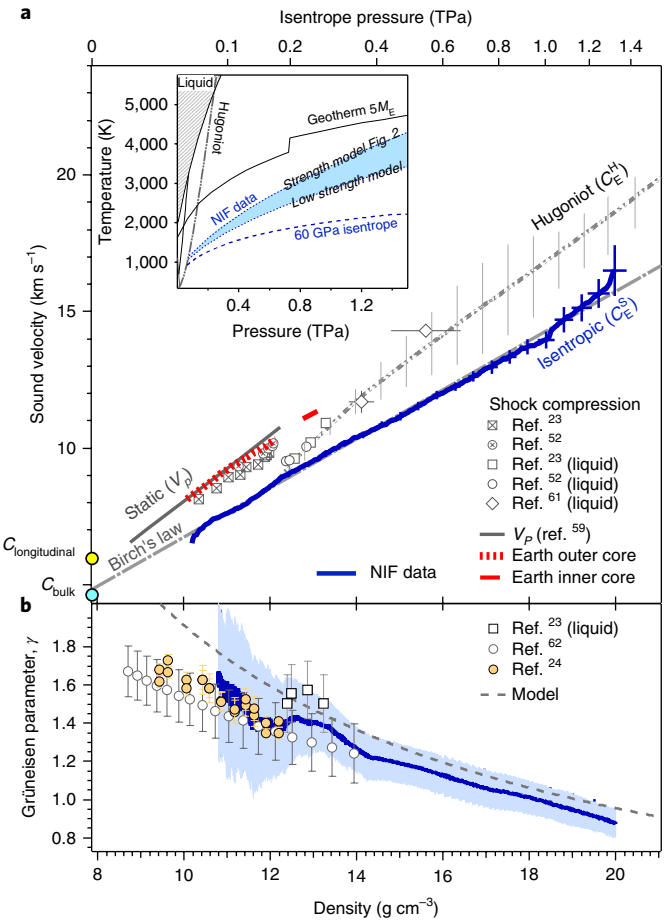

Fig. 3 | Sound velocity and Grüneisen parameter as a function of density for iron. a, Measured Eulerian bulk sound velocity, C_E^S, along an isentropic compression path (bold blue curve) is consistent with a linear Birch's law dependency (grey long-dashed curve)[22], where C_E^S (in km s^{-1}) = −2.2591 + 0.89941 × ρ (in g cm^{-3}). Error bars: 1σ. Pressure along the isentrope is shown on the top axis. Also plotted are the average longitudinal acoustic wave speeds (V_P) from static[59] (grey curve) and shock experiments (crossed squares[23] and crossed circles[52]). V_P data for the Earth's inner (red) and outer (red dashed) core are also shown[60]. Bulk sound speed measurements from shock melt experiments, C_E^H, are shown as open squares[23], open circles[52] and open diamonds[61]. The calculated bulk sound speed along the Hugoniot is shown as the grey short-dashed curve (see Methods). The ambient-pressure longitudinal and bulk sound speeds are labelled as yellow and cyan circles, respectively[19]. Inset: T–P plot for Fe with solid–solid phase boundaries, the calculated high-pressure melt line[19] (grey lines), the calculated Hugoniot and the isentrope from an initial 60 GPa shock state. Also shown is the calculated geotherm for a 5 Earth-mass planet[1]. The range of possible temperatures for the NIF data is represented as a solid blue shaded region where the upper temperature limit was calculated with the strength model used for the P–ρ analysis in Fig. 2 (see Supplementary Fig. 2b). The lower temperature limit represents the heating that results if we consider a strength model based on extrapolated static data (see Supplementary Fig. 2c). See Methods for details. **b**, Grüneisen parameter (γ) as a function of density, calculated from comparison between the isentrope and Hugoniot curves in Fig. 2, is plotted against previous measured values under static (open[62] and orange[24] circles) and shock compression (open squares[23]) (see Methods). Error bars: 1σ. The dashed curve is the $\gamma(\rho)$ dependency predicted in ref. [16].

(Fig. 4 and Supplementary Fig. 6). Our study provides a firmer basis for establishing the properties of the end-member case of a pure iron planet. Furthermore, our study demonstrates the capability for

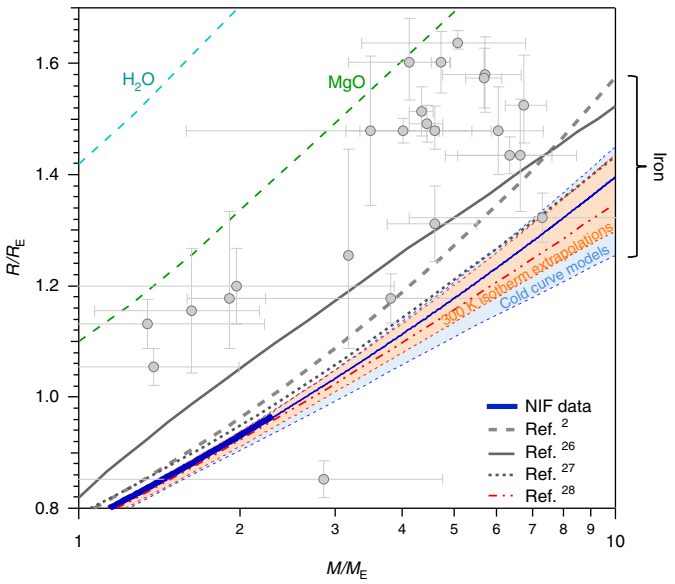

Fig. 4 | Mass–radius relationships for homogeneous-composition planets. Calculations for Fe (based on our data, where 1σ error bars are within the width of the line, bold blue). The thin blue line represents extrapolation of the NIF data using a linear Birch's law dependency of sound speed with density (grey long-dashed curve in Fig. 3). The range of Fe EOS models for $M/M_E = 10$ is highlighted on the right-hand axis. The orange and blue regions represent the range of uncertainty in extrapolation from low-pressure static data using phenomenological EOS models and the spread of first-principles cold curve calculations (see Supplementary Fig. 5). Representative previously reported mass–radius curves for Fe are also plotted (grey curve[26], grey dashed curve[2], grey dotted curve[27] and red dashed-dotted curve[28]). A more complete comparison with recent published mass–radius curves for Fe is shown in Supplementary Fig. 6. Also shown are the mass–radius curves for hypothetical MgO (dashed green) and H_2O (dashed blue) planets[2]. The circles represent measurements of selected transiting super-Earths, with error bars as reported in ref. [29]. M_E and R_E are the mass and radius of the Earth, respectively.

determination of EOSs and other key thermodynamic properties of planetary core materials at pressures well beyond those of conventional static techniques. Such information is crucial for advancing our understanding of the structure and dynamics of large rocky exoplanets and their evolution. Future experiments will extend the study of planetary materials to several TPa.

Methods

Target design. The target consists of an Au cylinder (or 'hohlraum') (11 mm in length and 6 mm in diameter with 25-μm-thick walls), two laser entrance holes (LEHs) at the ends (4.5 mm in diameter) and a Cu/Fe step sample affixed to the hohlraum wall over a 3-mm-diameter hole (inset to Supplementary Fig. 1a). Laser beams ($n = 176$) were focused though the LEHs and onto the inner walls of the hohlraum. Each beam had a shaped laser power history designed to generate an initial 60 GPa (0.06 TPa) shock within the Fe sample before subsequent ramp compression to TPa pressures (Fig. 1 and Supplementary Fig. 1a). The hohlraum was filled with 0.1 atmospheres of neopentane gas (C_5H_{12}), which restricted the flow of ablated Au towards the hohlraum axis and which would otherwise have reduced laser coupling and the peak achievable sample pressure. The gas was contained inside the hohlraum with 0.6-μm-thick polyimide layers, which covered the LEHs. X-rays generated by laser ablation of the hohlraum walls were emitted, reabsorbed and remitted in a process that resulted in a near blackbody distribution[32]. The X-rays were absorbed by and ablated the Cu foil portion of the target package in a process that imparted a time-varying and spatially uniform pressure wave into the Cu/Fe step target assembly. The target package consisted of a ~40-μm-thick Cu layer and a step target of iron with thicknesses in the 83–116 μm range. The high-purity (99.995%) Fe steps were manufactured using a vapour-deposition and shadow-masking technique, which produced fully dense layers (7.875 g cm^{-3}) to within 0.6%[33]. Pole figure measurements showed that the Fe BCC crystal structure was orientated with the [110] axis in the growth (pressure loading) direction with random orientation in-plane. Metrology of the sample surface showed that the roughness was <0.1 μm, the thickness gradients were <1% and step heights were accurate to within ~0.1 μm.

Velocity interferometry. A 660 nm Doppler interferometer known as a 'velocity interferometer system for any reflector' (VISAR) was used to measure the Fe free-surface velocity, $u_{fs}(t)$, for each sample thickness[34]. The VISAR system imaged across the Fe steps in one dimension with ~30 μm spatial resolution, and provided continuous velocity-versus-time data over a 1 mm field of view. Two VISAR channels with different velocity sensitivities were used simultaneously to resolve any velocity ambiguities that could arise if the rate of target velocity change exceeded the time response of the system. VISAR fringe movement was directly proportional to the velocity of the Fe free surface and was resolved in time with a streak camera (inset in Supplementary Fig. 1b). The streak camera had ~200–300 time elements across the sweep window, which equated to a ~40–150 ps delta-function resolution for the time windows used in our experiments (~5 pixels on the sweep record). However, the time difference between temporal events on the same streak record and at spatially distinct locations (for example, the time separation between velocity profiles from different Fe steps) is known to a higher precision than the streak camera delta-function resolution. We estimated, from peak-fitting a sequence of light pulses with a known temporal separation, that the time difference between two distinct time events can be measured to one part in a thousand or ~1–2 pixels on the streak record. We verified this with calculated multi-stepped $u_{fs}(t)$ data for a material with a known EOS. A one-dimensional Gaussian blur was applied along the time axis of a simulated VISAR interferogram to account for the finite streak camera delta-function time resolution. A Lagrangian analysis was then employed to the extracted $u_{fs}(t)$ data, and the input EOS was reproduced to within ~0.5% in pressure at 1,000 GPa. This confirmed that the accuracy with which we can correlate $u_{fs}(t)$ for two different steps is better than the delta-function time resolution. In addition, when we cross-correlated the $u_{fs}(t)$ traces measured by the two independent VISAR systems used on each shot (with different temporal sweep windows and different etalons), the temporal separation between velocity profiles from different steps agreed to within a 1–2 pixel uncertainty.

***P*$_x$–ρ and sound speed analysis.** A Lagrangian analysis[35–38] following the method of ref. [39] was used to translate the $u_{fs}(t)$ data (from all four Fe thicknesses) into Lagrangian sound speed ($C_L(u)$, where u is the particle velocity) and P_x–ρ relations that quantified the loading path (Supplementary Fig. 3a). $C_L(u)$ data for three shots are shown in the inset to Fig. 1. Two VISAR channels were used for each shot and each channel was treated as an independent measurement. $C_L(u)$ and its uncertainty $\sigma_{C_L}(u)$ were obtained from thickness and velocity-versus-time data by linear regression using errors determined by our measurement accuracies (discussed below). The uncertainty was propagated by calculating the weighted mean average of all three shots, $C_L(u) = \sum_j \frac{C_{L,j}}{\sigma^2_{C_L}(u)} / \sum_j \frac{1}{\sigma^2_{C_L}(u)}\Big|_u$, as shown by the blue curve in Fig. 1, where j is the shot number. The uncertainty in the average value was chosen from the maximum of the uncertainty in the mean and the weighted standard deviation. $C_L(u)$ and $\sigma_{C_L}(u)$ were integrated to obtain $P_x = P_H + \rho_0 \int_{u_H}^{u} C_L \mathrm{d}u$ and $\rho = \rho_0 \left(1 - \frac{\rho_H - \rho_0}{\rho_H} - \int_{u_H}^{u} \frac{\mathrm{d}u}{C_L}\right)^{-1}$ and their uncertainties $\sigma_{P_x} = \sigma_{P_{x,H}} + \rho_0 \int_{u_H}^{u} \sigma_{C_L} \mathrm{d}u$ and $\sigma_\rho = \frac{\rho^2}{\rho_0} \int_{u_H}^{u} \frac{\sigma_{C_L}}{C_L^2} \mathrm{d}u$. Here, P_H, ρ_H and u_H are the pressure, density and particle velocity, respectively, associated with the initial 60 GPa shock Hugoniot state[21]. Uncertainties are propagated though the integrals linearly, rather than in quadrature, because they appear to be strongly correlated rather than random. This method of uncertainty propagation allows the direct propagation of experimental uncertainties. Sound speed analysis over the three steps (four thicknesses) showed simple wave behaviour, suggesting that the material response was not time-dependent within the experimental uncertainties. Release waves from the Fe–vacuum interface significantly perturbed the incoming ramp wave. Extensive tests using simulated data confirmed that the Lagrangian analysis accurately corrects for these wave interactions.

Lagrangian analysis assumes isentropic and reversible flow. However, for experiments with an initial shock, the thermodynamic compression path is not reversible. Regions of the Fe sample close to the free surface that experience shock compression follow an isentropic release path not constrained by these measurements. We modified the Lagrangian analysis over previous implementations[15] to use an EOS model within this released region. We assume the release isentrope below 60 GPa is described correctly by Sesame EOS table 2150 (ref. [21]; see the 'model' curve in the inset of Fig. 1). Tests on simulated data showed that the determined high-pressure response of Fe is not sensitive to the low-pressure isentropic release model used.

In our experimental design, the 60 GPa shock wave compressed the sample into the high-pressure HCP phase before subsequent ramp compression to peak pressure. Hydrocode simulations showed that after this initial shock reached the Fe free-surface and, at times before the arrival of the ramp compression wave, a pressure release wave caused a ~3 μm thickness of Fe at the Fe–vacuum interface to decompress along a release isentrope and across lower-pressure $\epsilon \rightarrow \gamma$ and $\gamma \rightarrow \alpha$ phase boundaries. To determine whether the volume change associated with these

low-pressure phase transformations affected the bulk P_x–ρ determination, we used the hydrocode Hyades[40] and Sesame EOS table 2150 for Fe to simulate shot N150701 (ref. [21]). The Sesame EOS contains a full description of Fe equilibrium phase boundaries. Using simulated $u_{fs}(t)$ data from several thicknesses, we determined the P_x–ρ response using the Lagrangian analysis method and compared it with P_x–ρ values determined within the bulk from an internal tracer layer in the simulation. The difference in these values was ~0.5% in pressure at 1,000 GPa. We consider this an upper limit, as at high strain rates, phase transformations in Fe are kinetically inhibited[16].

Error analysis. The measurement of sound speed is dominated by the following random uncertainties:

(1) Uncertainty in Fe step height ($\delta x_{\mathrm{StepHeight}}$). Individual Fe step-thickness measurements were obtained through imaging white light interferometry techniques, which provided height differences between measurements from the rear (flat portion) and front (stepped portion) of the sample. This produced a two-dimensional thickness map across the sample surface. The measurements for step height used in our study are characterized by the difference between average values of the statistical distribution of thickness measurements for each step, with 1σ uncertainties. For all targets, $\delta x_{\mathrm{StepHeight}}$ values were determined to within an uncertainty of 0.04–0.17 μm. Systematic uncertainties in step-height measurement (~nm) were small as the white light interferometer was calibrated by gauge blocks of known thickness.

(2) Uncertainty in velocity determination (δu). The imaging-VISAR diagnostic provides continuous $u_{fs}(x,t)$ data along a one-dimensional line at the target plane[34]. For each Fe step, the average free-surface velocity in time, $u_{fs}(t)=\sum_{x=0}^{\mathrm{StepWidth}} u_{fs}(x,t)$, with random uncertainty $\delta u_{fs}(t)$, is determined by calculating the average phase shift and standard deviation across the full step width. Random uncertainties in the measurement of u_{fs} at any time on the trace can arise from (1) variations in the sample thickness resulting in compression wave arrival at different times across the step width and (2) random frequency structure on VISAR fringes due to random intensity laser speckle, which can shift the central position of a fringe[41]. In our analysis, δu was determined by comparing the two independent VISAR channels for a single experiment. δu_{fs} was scaled until 1σ of the error bars overlapped between the two datasets. Using this approach, $\delta u_{fs}=20$–$44\,\mathrm{m\,s^{-1}}$ (0.9–3.5% of a fringe shift).

(3) Uncertainty in time (δt). Random uncertainties in velocity result in random uncertainties in timing. In the original approach, δt was determined by comparing the two VISAR channels used in each experiment where the % velocity per fringe error was scaled until the 1σ error bars overlap. However, this appears to be an underestimate. Instead, in our analysis, δt was taken as equal to two time pixels in the velocity measurement and was therefore directly related to the VISAR streak camera sweep rate. Using this approach, $\delta t=20$–66 ps.

For convenience, these random uncertainties were then treated as uncertainties in distance (δx) as follows,

$$\delta x^2=(\delta x_{\mathrm{StepHeight}})^2+(\delta t\times C_{\mathrm{L}})^2+\left(\frac{\delta u\times C_{\mathrm{L}}}{\mathrm{d}u\,/\,\mathrm{d}t}\right)^2 \quad (1)$$

where C_{L} is the experimentally determined Lagrangian sound speed. All data and uncertainties were averaged in $C_{\mathrm{L}}(u)$ space (Fig. 1 inset, bold blue curve). This average was then used to calculate the average P_x–ρ curve (Supplementary Fig. 3a).

Reduction of the P_x–ρ data to an isentropic P–ρ path. Owing to the uniaxial compression geometry in our experiments, we measured longitudinal stress, P_x. To transform the measured P_x–ρ path to an isentropic P–ρ path, it was necessary to correct for (1) the deviatoric stress offset associated with relating the measured longitudinal stress to an equivalent hydrostatic pressure, (2) the thermal pressure of the initial 60 GPa shock and (3) work heating due to the high-pressure strength of Fe.

(1) Deviatoric stress offset. In the analysis of ref. [42] using the Lévy–von Mises yield criterion[43], the measured longitudinal stress P_x is related to a hydrostatic pressure by

$$P=P_x-\frac{2}{3}Y(P) \quad (2)$$

where Y is the yield strength. $Y(P)$ is calculated from a high-pressure strength model for Fe (see below).

(2) Thermal pressure offset from 60 GPa shock. Pressure along the Hugoniot, P_{H}, is related to the pressure along the isentrope P_{S} assuming the Mie–Grüneisen relation[44],

$$P_{\mathrm{H}}-P_{\mathrm{S}}=\gamma\rho\,(E_{\mathrm{H}}-E_{\mathrm{S}}) \quad (3)$$

where γ is the Grüneisen parameter, and E_{H} and E_{S} are the internal energies along the Hugoniot and isentrope, respectively. γ is assumed to depend on volume only such that

$$\gamma=\gamma_0\left(\frac{\rho_0}{\rho}\right)^q \quad (4)$$

where $\gamma_0=2.33$ and $q=1.36$ for ϵ-Fe[16] (grey dashed line in Fig. 3b). Following this analysis, and with an estimated shock temperature of 965 K[21], to account for the thermal pressure associated with the initial 60 GPa shock, we applied a correction of −3.55 GPa to our P_x–ρ data.

(3) Thermal pressure offset due to work heating. If a material supports strength at high pressure, work heating results in a thermal pressure offset from the isentrope. As the high-pressure strength of iron is not well constrained experimentally (Supplementary Fig. 2), to correct for this thermal pressure offset we must make bounding assumptions about strength as a function of pressure. Following the analysis of ref. [42], plastic work heating is given by

$$\mathrm{d}W_P=\frac{1}{\rho_{\varepsilon,0}}\frac{2}{3}Y\,[\mathrm{d}\varepsilon_x-\mathrm{d}Y\,/\,2G(\rho)] \quad (5)$$

where $G(\rho)$ is the shear modulus, Y is the yield strength, $\rho_{\varepsilon,0}$ is the density at $P=0$ for the Fe ϵ-phase ($8.43\,\mathrm{g\,cm^{-3}}$)[21] and $\varepsilon_x=\ln(\rho/\rho_{\varepsilon,0})$. The calculated temperature rise due to work heating, as shown in the inset to Fig. 3a, was calculated by dividing equation (5) by the specific heat, C_V. Following the analysis of ref. [23],

$$C_V=D(T)+\beta_e\left(\frac{\rho_0}{\rho}\right)^{\gamma^e} \quad (6)$$

where $D(T)$ is the Debye function. $D(T)=3R$ for $T>\theta$, where R is the gas constant and θ is the Debye temperature. The relation is satisfied considering the 60 GPa shock temperature of 965 K, and θ for ϵ-Fe is estimated to be 322 K[16]. In equation (6), β_e is proportional to the density of electrons at the Fermi level, and γ^e (the electronic Grüneisen parameter) describes the volume dependence for the density of states. Values for β_e and γ^e were determined for Fe to be $90.8\,\mathrm{J\,Mg^{-1}\,K^{-2}}$ (refs [23,45]) and 1.34 (ref. [23]), respectively.

Plastic work heating causes the mean hydrostatic pressure to deviate from an isentrope by

$$P_{\mathrm{hyd}}-P_{\mathrm{s}}=\gamma\rho\int_0^{\varepsilon_x}\beta\mathrm{d}W_P \quad (7)$$

where β is the Taylor–Quinney factor, which describes the fraction of plastic work that partitions into the thermal energy of the system[46]. Here, $\beta=1$, which assumes all plastic work is used to heat the material[47].

We extrapolate the shear modulus $G(\rho)$ data for Fe from static compression (23–210 GPa) using the functional form described in ref. [48], and assume,

$$Y'_P=\frac{G'_P}{G_0}Y_0 \quad (8)$$

where Y'_P and G'_P are the derivatives with respect to pressure, respectively. Y_0 is the yield strength and G_0 is 83 GPa[48]. The relation in equation (8) is used within the Steinberg–Cochran–Guinan constitutive model developed to describe high-strain-rate strength in metals[49]. To account for the pressure offset from an isentrope due to the high-pressure strength of Fe, we consider three cases for Y'_P:

(1) High-strength model. Based on low-pressure data within the Fe α-phase, we expect a strain-rate-dependent increase of Y_0 (ref. [50]). To account for this, we vary Y_0 in equation (8) so that the calculated Y'_P is consistent with the high strain-rate estimates of refs [17,51] (see Supplementary Fig. 2a). The datum of ref. [17] is not a direct measurement of strength and is described by the authors as an upper limit. Here, $Y_0=Y_{0,\mathrm{Static}}\times 8.2$, where $Y_{0,\mathrm{Static}}=1.45$ GPa. Using this Y'_P dependency, the calculated deviatoric stress offset (equation (2)) and thermal pressure due to work heating (equations (5) and (7)) are also plotted. The corrected P–ρ isentrope using this strength model is shown as a green dotted–dashed curve in Supplementary Fig. 3b. As the calculated isentrope is more compressible than the static data at pressure up to 300 GPa, we consider this model unphysical over this pressure range.

(2) Intermediate-strength model (used in Fig. 2). In our analysis, Y_0 has an upper limit such that the corrected isentropic P–ρ curve is not more compressible than the isentrope determined from 300 K isotherm data (see inset of Supplementary Fig. 3b). Here, $Y_0=Y_{0,\mathrm{Static}}\times 1.8$. The corrected P–ρ isentrope using this strength model is shown as the blue curve in Fig. 2 and Supplementary Fig. 3b.

(3) Low-strength model. $Y_0=Y_{0,\mathrm{Static}}=1.45$ GPa in equation (8) to match the measured $Y(P)$ over the 50–220 GPa range (green circles in Supplementary Fig. 2c). The corrected P–ρ isentrope using this strength model is shown as the black dashed curve in Supplementary Fig. 3b.

Grüneisen parameter determination. The Grüneisen parameter (Fig. 3b), γ, may be determined by comparing the Hugoniot and measured isentrope for Fe using the Mie–Grüneisen expression[44]

$$\gamma = V\left(\frac{P_H - P_S}{E_H - E_S}\right)_V = V\left(\frac{\alpha K_T}{C_V}\right) \quad (9)$$

The internal energy along the isentrope, $E_S = -\int_{V_0}^{V} P_S dV$, where V is the volume, S represents isentropic conditions and the subscript 0 represents ambient conditions. As the isentrope is calculated only above the initial 60 GPa shock ($\rho \sim 10.1\,g\,cm^{-3}$), in calculating E_S, we assume the isentrope from $P_S = 0-60$ GPa is described correctly by Sesame EOS table 2150 (ref. [21]). The energy along the Hugoniot is defined from the Rankine–Hugoniot relations as, $E_H = P_H(V_0 - V)/2$. α is the thermal expansivity, K_T is the isothermal bulk modulus and C_V is the specific heat.

Effect of melting along the Hugoniot in the determination of γ. Under shock compression, the onset and completion of melt in Fe occurs from $P \sim 222-260$ GPa, $T \sim 5{,}100-6{,}096$ K and $\rho \sim 12.181-12.467\,g\,cm^{-3}$ (ref. [52]). It is expected that there will only be small changes in α, K_T and V due to melt as the solid and liquid phases both have dense, closely packed structures. For example, based on theoretical studies, the volume of fusion of iron is predicted to be small above 100 GPa and to decline with pressure[53]. Changes in the above quantities between liquid and solid will also partially cancel in the determination of γ. As $C_V = \left.\frac{\delta E}{\delta T}\right|_V$, we also consider the effect energy change along the Hugoniot, due to the latent heat of fusion upon melting, has on the calculation of γ. Results from molecular dynamic simulations indicate that the change in energy at melt is <1% of ΔE_{H-S}, and lies well within the uncertainties of our calculation[54]. The Grüneisen parameter will be further modified if there are changes in the vibrational modes and electron excitations. At low temperatures, vibrational modes will be frozen out. At the high temperatures associated with extreme levels of compression along the Hugoniot, the population of free electrons increases and the ions eventually become free (heat capacity $3k_B/2$ per atom instead of $3k_B$ per atom). Based on atom-in-jellium calculations of ionization and displacement, and the Sesame EOS table for Fe[21], in the regime of these experiments, these effects are not expected to be significant.

Uncertainties in the determination of γ. The uncertainties in $\gamma(\rho)$ are directly related to the pressure uncertainties in the Hugoniot fit and the isentrope, where uncertainties in ΔP and ΔE in equation (9) are correlated. A P_H–ρ fit to Fe Hugoniot data is shown in Supplementary Fig. 4 with pressure residuals to the fit shown within the inset figure. Uncertainties in the Hugoniot fit were determined through standard deviation analysis of the pressure residuals. Our analysis was based on the scatter of the Hugoniot data and did not take into account reported experimental uncertainties. Additional uncertainties related to the high-pressure strength of Fe were not considered.

Bulk sound speed determination. Along the Hugoniot, the Eulerian bulk sound speed (Fig. 3), C_E^H, of Fe for $P > P_{melt}$ may be calculated by ref. [55]

$$(C_E^H)^2 = V^2\left[\left(\frac{\delta P}{\delta V}\right)_H\left[(V_0 - V)\frac{\gamma}{2V} - 1\right] + \frac{P\gamma}{2V}\right] \quad (10)$$

Here, $\left(\frac{\delta P}{\delta V}\right)_H$ is determined from the Hugoniot fit in Supplementary Fig. 4. $\gamma(\rho)$ is plotted in Fig. 3b. C_E^H for the Hugoniot is plotted as the grey short-dashed curve in Fig. 3a. The uncertainties in C_E^H are calculated from the uncertainties in the Hugoniot fit and the uncertainties in $\gamma(\rho)$.

The bulk sound speed along an isentrope is given by $C_E^S = V\sqrt{\left(\frac{-\delta P}{\delta V}\right)_S}$, where S represents isentropic conditions[56]. C_E^S along the calculated isentrope in Fig. 2 is plotted as the bold blue curve in Fig. 3a.

Pressure offset due to sample temperature. Supplementary Fig. 7 represents previous high-pressure studies that show the effect of temperature on the compressibility of Fe. Here, P–ρ data for Fe under static compression for different starting temperatures are plotted[57]. Also plotted are Hugoniot data and the more recent 300 K static data of ref. [10]. The high-temperature data of ref. [57], while scattered, give some measure of the effect of thermal pressure as a function of sample temperature. The estimate of thermal expansivity in that work is in agreement with estimates under shock compression[58]. Also shown in Supplementary Fig. 7 are three P–ρ curves from Sesame EOS table 2150 for Fe[21]: (1) a 300 K isotherm, (2) an isentrope following a 60 GPa shock ($T_{Shock} = 965$ K) and (3) an isentrope following a 140 GPa shock ($T_{Shock} = 2{,}900$ K). We used these three examples to quantify the effect temperature has on pressure and density at TPa pressures. The pressure offset from the isotherm as a function of density and pressure is shown as an inset in Supplementary Fig. 7. For a hypothetical homogeneous Fe 10-Earth-mass planet the central pressure is ~7 TPa, assuming Sesame EOS 2150 (refs [2,21]). At these pressures, the calculated percentage pressure offset due to the initial temperatures considered in Supplementary Fig. 7 is negligible.

Data availability. The data that support the plots within this paper and other findings of this study are available from the corresponding author upon reasonable request.

Received: 2 November 2017; Accepted: 5 March 2018;
Published online: 16 April 2018

References

1. Valencia, D., O'Connell, R. J. & Sasselov, D. Internal structure of massive terrestrial planets. *Icarus* **181**, 545–554 (2006).
2. Swift, D. C. et al. Mass–radius relationships for exoplanets. *Astrophys. J.* **744**, 59 (2012).
3. Wagner, F. W., Tosi, N., Sohl, F., Rauer, H. & Spohn, T. Rocky super-Earth interiors— Structure and internal dynamics of CoRoT-7b and Kepler-10b. *Astron. Astrophys.* **541**, A103 (2012).
4. Marcy, G. W. et al. Occurrence and core-envelope structure of 1–4x Earth-size planets around Sun-like stars. *Proc. Natl Acad. Sci. USA* **111**, 12655–12660 (2014).
5. Santos, N. et al. Constraining planet structure from stellar chemistry: the cases of CoRoT-7, Kepler-10, and Kepler-93. *Astron. Astrophys.* **580**, L13 (2015).
6. Gillon, M. et al. Seven temperate terrestrial planets around the nearby ultracool dwarf star TRAPPIST-1. *Nature* **542**, 456–460 (2017).
7. Noack, L. et al. Can the interior structure influence the habitability of a rocky planet? *Planet. Space Sci.* **98**, 14–29 (2014).
8. Foley, B. J. & Driscoll, P. E. Whole planet coupling between climate, mantle, and core: implications for rocky planet evolution. *Geochem. Geophys. Geosyst.* **17**, 1885–1914 (2016).
9. Marcus, R. A., Stewart, S. T., Sasselov, D. & Hernquist, L. Collisional stripping and disruption of super-Earths. *Astrophys. J. Lett.* **700**, L118 (2009).
10. Dewaele, A. et al. Quasihydrostatic equation of state of iron above 2 Mbar. *Phys. Rev. Lett.* **97**, 215504 (2006).
11. Cohen, R. E. & Mukherjee, S. Non-collinear magnetism in iron at high pressures. *Phys. Earth Planet. Inter.* **143**, 445–453 (2004).
12. Stixrude, L. Structure of Iron to 1 Gbar and 40 000 K. *Phys. Rev. Lett.* **108**, 055505 (2012).
13. Lazicki, A. et al. X-ray diffraction of solid tin to 1.2 TPa. *Phys. Rev. Lett.* **115**, 075502 (2015).
14. Amadou, N. et al. Probing iron at super-Earth core conditions. *Phys. Plasmas* **22**, 022705 (2015).
15. Smith, R. F. et al. Ramp compression of diamond to five terapascals. *Nature* **511**, 330–333 (2014).
16. Smith, R. F. et al. Time-dependence of the alpha to epsilon phase transformation in iron. *J. Appl. Phys.* **114**, 223507 (2013).
17. Ping, Y. et al. Solid iron compressed up to 560 GPa. *Phys. Rev. Lett.* **111**, 065501 (2013).
18. Ahrens, T. J. *Mineral Physics and Crystallography: a Handbook of Physical Constants* 143–184 (American Geophysical Union, Washington, DC, 1995).
19. Wang, J. et al. Ramp compression of iron to 273 GPa. *J. Appl. Phys.* **114**, 023513 (2013).
20. Vinet, P., Ferrante, J., Rose, J. & Smith, J. Compressibility of solids. *J. Geophys. Res. Solid Earth* **92**, 9319–9325 (1987).
21. Kerley, G. I. *Multiphase Equation of State for Iron.* Report No. SAND93-0027 (Sandia National Laboratory, 1993).
22. Birch, F. Composition of the Earth's mantle. *Geophys. J. Int.* **4**, 295–311 (1961).
23. Brown, J. M. & McQueen, R. G. Phase transitions, Grüneisen parameter, and elasticity for shocked iron between 77 GPa and 400 GPa. *J. Geophys. Res.* **91**, 7485–7494 (1986).
24. Murphy, C. A., Jackson, J. M., Sturhahn, W. & Chen, B. Grüneisen parameter of HCP-Fe to 171 GPa. *Geophys. Res. Lett.* **38**, L24306 (2011).
25. Anderson, O. L. The Grüneisen parameter for iron at outer core conditions and the resulting conductive heat and power in the core. *Phys. Earth Planet. Inter.* **109**, 179–197 (1998).
26. Zapolsky, H. S. & Salpeter, E. E. The mass–radius relation for cold spheres of low mass. *Astrophys. J.* **158**, 809–813 (1969).
27. Valencia, D., Ikoma, M., Guillot, T. & Nettelmann, N. Composition and fate of short-period super-Earths—the case of CoRoT-7b. *Astron. Astrophys.* **516**, A20 (2010).
28. Howe, A. R., Burrows, A. & Verne, W. Mass–radius relations and core-envelope decompositions of super-Earths and sub-Neptunes. *Astrophys. J.* **787**, 173 (2014).
29. Akeson, R. L. et al. The NASA exoplanet archive: data and tools for exoplanet research. *Publ. Astron. Soc. Pac.* **125**, 989–999 (2013).
30. Mocquet, A., Grasset, O. & Sotin, C. Very high-density planets: a possible remnant of gas giants. *Philos. Trans. R. Soc. A* **372**, 20130164 (2014).

31. Marcus, R. A., Sasselov, D., Hernquist, L. & Stewart, S. T. Minimum radii of super-earths: constraints from giant impacts. *Astrophys. J. Lett.* **712**, L73 (2010).
32. Moody, J. D. et al. Progress in hohlraum physics for the National Ignition Facility. *Phys. Plasmas* **21**, 056317 (2014).
33. Mirkarimi, P., Bettencourt, K., Teslich, N. & Peterson, S. Recent advances in the fabrication of very thick, multistepped iron and tantalum films for EOS targets. *Fusion Sci. Technol.* **63**, 282–287 (2013).
34. Celliers, P. M. et al. Line-imaging velocimeter for shock diagnostics at the OMEGA laser facility. *Rev. Sci. Instrum.* **75**, 4916–4929 (2004).
35. Fowles, R. & Williams, R. F. Plane stress wave propagation in solids. *J. Appl. Phys.* **41**, 360–363 (1970).
36. Cowperthwaite, M. & Williams, R. Determination of constitutive relationships with multiple gauges in nondivergent waves. *J. Appl. Phys.* **42**, 456–462 (1971).
37. Cagnoux, J., Chartagnac, P., Hereil, P., Perez, M. & Seaman, L. Lagrangian analysis. Modern tool of the dynamics of solids. *Ann. Phys.* **12**, 451–524 (1987).
38. Aidun, J. B. & Gupta, Y. M. Analysis of Lagrangian gauge measurements of simple and non-simple plane waves. *J. Appl. Phys.* **69**, 6998–7014 (1991).
39. Rothman, S. D. et al. Measurement of the principal isentropes of lead and lead-antimony alloy to ~400 kbar by quasi-isentropic compression. *J. Phys. D* **38**, 733–740 (2005).
40. Larsen, J. T. & Lane, S. M. HYADES—a plasma hydrodynamics code for dense plasma studies. *J. Quant. Spectrosc. Radiat. Transf.* **51**, 179–186 (1994).
41. Erskine, D. Speckle-adaptive VISAR fringe analysis technique. *AIP Conf. Proc.* **1793**, 160017 (2017).
42. Fowles, G. R. Shock wave compression of hardened and annealed 2024 aluminum. *J. Appl. Phys.* **32**, 1475–1487 (1961).
43. Hill, R. *The Mathematical Theory of Plasticity* (Oxford Univ. Press, New York, 1950).
44. Ahrens, T. J. in *High-Pressure Shock Compression of Solids* 75–114 (Springer, New York, 1993).
45. Brown, J. M. & McQueen, R. G. in *High-Pressure Research in Geophysics* (eds Akimoto, S. & Manghnani, M. H.) 611–623 (Riedel, Boston, 1982).
46. Taylor, G. I. & Quinney, H. The latent energy remaining in a metal after cold working. *Proc. R. Soc. Lond. A* **143**, 307–326 (1934).
47. Zaera, R., Rodriguez-Martinez, J. A. & Rittel, D. On the Taylor–Quinney coefficient in dynamically phase transforming materials. Application to 304 stainless steel. *Int. J. Plast.* **40**, 185–201 (2013).
48. Gleason, A. E. & Mao, W. L. Strength of iron at core pressures and evidence for a weak Earth's inner core. *Nat. Geosci.* **6**, 571–574 (2013).
49. Steinberg, D. J., Cochran, S. G. & Guinan, M. W. A constitutive model for metals applicable at high-strain rate. *J. Appl. Phys.* **51**, 1498–1504 (1980).
50. Smith, R. F. et al. High strain-rate plastic flow in Al and Fe. *J. Appl. Phys.* **110**, 123515 (2011).
51. Huntington, C. M. et al. Investigating iron material strength up to 1 Mbar using Rayleigh–Taylor growth measurements. *AIP Conf. Proc.* **1793**, 110007 (2017).
52. Nguyen, J. H. & Holmes, N. C. Melting of iron at the physical conditions of the Earth's core. *Nature* **427**, 339–342 (2004).
53. Zhang, W.-J., Liu, Z.-Y., Liu, Z.-L. & Cai, L.-C. Melting curves and entropy of melting of iron under Earth's core conditions. *Phys. Earth Planet. Inter.* **244**, 69–77 (2015).
54. Luo, F., Cheng, Y., Chen, X.-R., Cai, L.-C. & Jing, F.-Q. The melting curves and entropy of iron under high pressure. *J. Chem. Eng. Data* **56**, 2063–2070 (2011).
55. McQueen, R. G., Marsh, S. P. & Fritz, J. N. Hugoniot equation of state of twelve rocks. *J. Geophys. Res.* **72**, 4999–5036 (1967).
56. Duffy, T. S. & Ahrens, T. J. in *High-Pressure Research: Application to Earth and Planetary Sciences* 353–361 (Terra Scientific Publishing Company, Tokyo and American Geophysical Union, Washington D.C., 1992).
57. Dubrovinsky, L. S., Saxena, S. K., Tutti, F., Rekhi, S. & LeBehan, T. In situ X-ray study of thermal expansion and phase transition of iron at multimegabar pressure. *Phys. Rev. Lett.* **84**, 1720–1723 (2000).
58. Duffy, T. S. & Ahrens, T. K. Thermal expansion of mantle and core materials at very high pressures. *Geophys. Res. Lett.* **20**, 1103–1106 (1993).
59. Antonangeli, D. & Ohtani, E. Sound velocity of HCP-Fe at high pressure: experimental constraints, extrapolations and comparison with seismic models. *Progress. Earth Planet. Sci.* **2**, 3 (2015).
60. Dziewonski, A. M. & Anderson, D. L. Preliminary reference Earth model. *Phys. Earth Planet. Inter.* **25**, 297–356 (1981).
61. Sakaiya, T. et al. Sound velocity and density measurements of liquid iron up to 800 GPa: a universal relation between Birch's law coefficients for solid and liquid metals. *Earth Planet. Sci. Lett.* **392**, 80–85 (2014).
62. Dubrovinsky, L. S., Saxena, S. K., Tutti, F., Rekhi, S. & LeBehan, T. Gruneisen parameter of epsilon-iron up to 300 GPa from in-situ X-ray study. *Am. Mineral.* **85**, 386–389 (2000).

Acknowledgements

We thank the laser and target fabrication staff of the NIF, G. Wisoff, M. Herrmann and B. Goldstein. Beam time was granted through the Science Use of NIF programme. This work was performed under the auspices of the US Department of Energy by Lawrence Livermore National Laboratory under contract number DE-AC52-07NA27344, with additional support from the Department of Energy, University of California and Miller Institute for Basic Research in Science. This research has made use of the NASA Exoplanet Archive, which is operated by the California Institute of Technology, under contract with the National Aeronautics and Space Administration under the Exoplanet Exploration Program.

Author contributions

R.F.S., D.E.F., D.G.B. and J.H.E. designed, executed and analysed the data from the ramp compression experiments. P.M.C. helped with the analysis of the VISAR data. S.J.A. and A.F.P. performed hydrocode modelling to help determine the systematic uncertainties in the measurement. T.S.D., J.K.W. and D.C.S. performed the comparisons of experimental data with EOS models and theory. R.G.K and G.W.C. helped interpret the data.

Competing interests

The authors declare no competing interests.

Additional information

Supplementary information is available for this paper at https://doi.org/10.1038/s41550-018-0437-9.

Reprints and permissions information is available at www.nature.com/reprints.

Correspondence and requests for materials should be addressed to R.F.S.

Publisher's note: Springer Nature remains neutral with regard to jurisdictional claims in published maps and institutional affiliations.